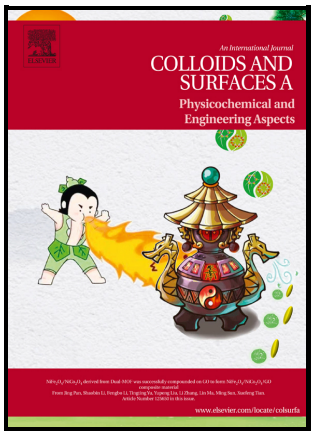

Compound distribution, structural analysis and nanomechanical properties of nanofibers loaded with high-oleic palm oil nanoemulsions for packaging application

Leidy Ricaurte, María de Jesús Perea-Flores, Juan Vicente Méndez-Méndez, Patricio Román Santagapita, Maria Ximena Quintanilla-Carvajal

PII: S0927-7757(21)02017-3

DOI: https://doi.org/10.1016/j.colsurfa.2021.128148

Reference: COLSUA128148

To appear in: *Colloids and Surfaces A: Physicochemical and Engineering Aspects*

Received date: 29 April 2021
Revised date: 14 December 2021
Accepted date: 16 December 2021

Please cite this article as: Leidy Ricaurte, María de Jesús Perea-Flores, Juan Vicente Méndez-Méndez, Patricio Román Santagapita and Maria Ximena Quintanilla-Carvajal, Compound distribution, structural analysis and nanomechanical properties of nanofibers loaded with high-oleic palm oil nanoemulsions for packaging application, *Colloids and Surfaces A: Physicochemical and Engineering Aspects,* (2021) doi:https://doi.org/10.1016/j.colsurfa.2021.128148

Compound distribution, structural analysis and nanomechanical properties of nanofibers loaded with high-oleic palm oil nanoemulsions for packaging application

Leidy Ricaurte[1], María de Jesús Perea-Flores[2], Juan Vicente Méndez-Méndez[2], Patricio Román Santagapita[3], Maria Ximena Quintanilla-Carvajal[1*]

[1]Doctorate program in Biosciences, Facultad de Ingeniería, Universidad de La Sabana, km 7 vía autopista Norte, Bogotá, Colombia

[2]Laboratorio de Microscopía Confocal, Centro de Nanociencias y Micro y Nanotecnología, Unidad Profesional 'Adolfo López Mateos', IPN, Luis Enrique Erro S/N, Zacatenco, C. P. 07738, Mexico City, Mexico

[3]Departamentos de Industrias y Química Orgánica, Facultad de Ciencias Exactas y Naturales, Universidad de Buenos Aires, Buenos Aires, Argentina

*Corresponding author: e-mail address: maria.quintanilla1@unisabana.edu.co

Abstract

The effect of the HOPO concentration on the morphology, fiber diameter, oil load and distribution, protein structure, protein-oil colocalization, and nanomechanical properties of the NFs were evaluated. We obtained smooth and defect-free NFs with diameters in range of 77-94 nm. Fourier-transform infrared spectroscopy was used as a reliable method to confirm oil load and protein structure after electrospinning. β-turn, β-sheet, α-helix, and triple helical structures were quantified. Confocal laser scanning microscopy was used to analyze colocalization, and results revealed a high distribution of NE droplets along the NFs and high oil-protein colocalization (overlap coefficient of ~0.63). The nanomechanical properties of the NE-loaded NFs demonstrated that at higher HOPO concentrations, the elastic modulus decreased. Likewise, homogeneity and synergy between compounds were observed. The adhesion properties of NE-loaded NFs were associated with their sticky surface, which was attributed to presence of HOPO. The NE-loaded NFs presented suitable physical properties for edible packaging.

Keywords:

Electrospinning, protein structure, colocalization, mechanical properties, biofilm.

1. Introduction

Owing to their affordable cost and suitable properties, non-biodegradable and non-renewable polymers are currently used for food applications; however, their disposal and accumulation present environmental and social threats [1]. A new approach, which relies on the use of eco-friendly polysaccharides and proteins, has been proposed for the development of sustainable and edible packaging, such as coatings and film formulations.

Gelatin is an animal protein that has been used to form bulk and nanostructured films. Nanostructures such as nanofibers (NFs) have been studied for medical, pharmaceutical, antimicrobial, encapsulation, and packaging applications. The last two types of applications have been combined to produce edible packaging using gelatin-based NFs that encapsulate high-oleic palm oil (HOPO) nanoemulsions (NEs) and macroemulsions via electrospinning. The emulsion droplet size significantly affected the fiber diameter and the crystal structure of the emulsion-loaded NFs [2]. Furthermore, high oil encapsulation was achieved via electrospinning to produce NFs with good nutritional and functional properties. NF-based films were formulated to contribute to the nutrition levels of the packaged foods. Hence, we aimed to develop a NE-functionalized NF-based biofilm with high HOPO load.

The conformational structure of proteins is the most important factor for successful electrospinning; moreover, linear protein chains are required to achieve suitable stretching and fiber formation [3]. Some authors have reported that electrospinning caused changes in the molecular conformation in electrospun gelatin [4]. Indeed, HOPO NEs could affect the final NF structure, and thus, both the protein structure and HOPO load should be studied. Fourier-transform infrared (FTIR) spectroscopy and confocal laser scanning microscopy (CLSM) are non-destructive powerful methods for analyzing all types of compounds, including hydrophilic and lipophilic substances, proteins, and carbohydrates. FTIR spectroscopy can be used to elucidate the composition and structure of compounds and CLSM can be used to determine the distribution, structure, and colocalization of compounds, via the bonding of fluorochromes with chemical groups. The compound distributions inside NFs could contribute to the better understanding of the mechanical properties of NF-based films. Nanoindentation is a technique that provides nanometer scale details on the biopolymer surface behavior under deformation [5]. Therefore, this information is relevant for using nanostructured films for packaging applications due to mechanical methods have been extensively stablished for bulk materials.

Therefore, the aim of this study was to analyze the effect of the HOPO concentration in NE-loaded gelatin-based NFs on the protein structure, oil loading and distribution, protein-oil colocalization, and their relationship with nanomechanical properties, such as the elastic modulus (E), reduced modulus (E_r), force of adhesion, and work of adhesion ($\Delta\gamma$).

2. Materials and methods

HOPO (Hacienda la Cabaña, Colombia) was donated by the Center for Research on Palm Cultivation, (Colombia), whey was obtained from a local supermarket, soy lecithin was purchased from Bell Chem (Colombia), bromelain with an activity of 1200 GDU/g was procured from MP biomedicals (USA), gelatin type A (approximately 280 bloom) was supplied by Cympa S.A.S (Colombia), acetic acid (99.8% purity) was acquired from Honeywell (USA). The fluorochromes (Nile red and Fluorescein isothiocyanate (FTIC)) were supplied by Sigma Aldrich (United States). Distilled water was used for all experiments.

2.1. The strategy to produce nanofibers loaded with HOPO nanoemulsions

2.1.1. Nanoemulsion preparation

2.1.1.1. Coarse emulsion preparation

A hand blender (Oster, Columbia) was used to homogenize four coarse emulsions (5%, 10%, 15%, or 20% w/w of HOPO) that were prepared as follows. First, 10% w/w sweet whey was dissolved in water, and then, HOPO and 10% w/w lecithin regarding HOPO concentration were mixed manually and added to the water-whey mixture. Subsequently, 10 μg/mL Nile red was added to the emulsions for CLSM oil analysis (more details in section 2.6.2). The total mixing time of all the ingredients was approximately 2 min.

2.1.1.2. Nanoemulsion preparation

HOPO NE with HOPO concentrations of 0%, 5%, 10%, 15%, and 20% w/w, hereafter NE0, NE5, NE10, NE15, and NE20, respectively, were obtained via microfluidization using a previously published method [6]. Briefly, each coarse emulsion was homogenized using an LM10 (Microfluidics, UK) microfluidizer at 20 000 psi for three cycles. The average droplet sizes (ADSs), polydispersity indices (PdIs), and zeta potentials (ζ) of the NEs were determined

using a Zetasizer Nano ZS, Malvern Instruments (UK) dynamic light scattering (DLS) instrument and 1:1000 (v/v) water dilutions. All measurements were performed in triplicate.

2.1.2. Gelatin solution preparation

The same gelatin solution formulation, which was obtained using the optimum condition established by Ricaurte et al. (2019) (25% w/w gelatin was slowly added to water at 50 °C under magnetic shaking until total dissolution) was used for all experiments. Subsequently, the temperature of the solution was decreased to 40 °C for suitable enzyme action and 0.2 GDU bromelain (approximately 70 μL) was incorporated into the gelatin solution (the enzyme preparation procedure is described in the literature [7]). After 5 min, the enzymatic reaction was stopped by placing the mixture in a water bath at 90 °C for 10 min. The bromelain enzyme was added to reduce the solution viscosity for assuring a continuous process (the gelation inside electrospinning is also avoided). The protein was stained with 100 ng fluorescein isothiocyanate (FITC)/1 μg of protein for CLSM analysis (section 2.6.2), and then the samples were cooled to 35 °C and subjected to electrospinning. The gelatin solution was not used into the aqueous phase of NEs production to prevent the gelation inside microfluidizer.

2.1.3. Preparation of electrospun solutions

Mixtures of gelatin solution and 5%, 10%, 15%, and 20% w/w HOPO NEs with the gelatin-to-NE mass ratio of 0.89:0.11 were used to obtain electrospun NF solutions according to the optimum formulations reported by Ricaurte et al. (2020). In addition, a NE-free gelatin solution was electrospun and was used as control.

2.1.4. Processing conditions of electrospinning

The Fluidnatek® LE-10 (Bioinicia, Spain) electrospinning equipment was fitted with a plastic syringe (capacity of 20 mL and outer diameter of 1/16″), syringe pump, high voltage source, and flat stainless-steel collector (200 mm× 200 mm). The equipment was operated at a constant flow rate of 0.1 mL/min, and the tip-collector distance was 7 cm. The voltage applied was 14 kV, when the Taylor's cone was observed. The electrospinning conditions were maintained at 15 °C and 75% humidity throughout the experiments.

2.2. NF morphology and diameter

The morphology and fiber diameter (D_f) of the NFs were determined using a JSM 7800f (JEOL, Japan) microscope operated at 3 kV in low-vacuum mode. The samples were covered with gold for 20 s and observed at ×20 000 magnification. To quantify D_f, five micrographs were acquired for each sample.

2.3. Oil distribution inside the NFs

2.3.1. Attenuated total reflection and Fourier-transform infrared spectroscopy

The band presences and intensity differences owing to the oil concentration (0-20% w/w HOPO) in the NF matrices were determined using a FTIR-IR module coupled with a confocal (HORIBA Jobin Yvon, USA) micro-RAMAN spectrometer. Scanning was performed in the wavenumber range of 4000-400 cm^{-1} at a spectral resolution of 4 cm^{-1}. Each measurement was performed using 32 scans employing an attenuated total reflection (ATR) lens with a magnification of ×36. The Spectragryph (version 1.2.13, Friedrich Menges, Germany) software was used to obtain the second-derivative spectra, band heights, and integration by area of the samples. The second-derivative spectra were calculated using a five-point smoothing point Savitzky–Golay algorithm to determine the changes in the secondary structure of gelatin in the wavenumber range of 1600-1700 cm^{-1} [8]. The conformational structure of gelatin in the NFs was also determined, and the percentages of α-helix (1653 cm^{-1}), β-sheet (1637 cm^{-1}), and β-turns (1670 and 1690 cm^{-1}) structures were calculated from their relative areas [9]. Protein integrity was analyzed using the intensities of the bands at 1235 and 1450 cm^{-1}. The ratio between the intensities of these bands was used as relationship with the presence of triple helical structure from gelatin protein in NFs. Lastly, integration by area was performed for the peak at 2930 cm^{-1}, which corresponded to the C−H (−CH_2–) asymmetric stretching vibrations (Rohman et al. 2014) and those peaks at 1745 and 2855 cm^{-1}, which were associated with the presence of HOPO (Poiana et al. 2015). The 1745 cm^{-1}:2930 cm^{-1} and 2855 cm^{-1}:2930 cm^{-1} peak absorption ratios were calculated and were used as convenient oil loading indices in NF regarding gelatin protein.

2.3.2. CLSM analysis

The distribution of HOPO in the NEs and HOPO-protein colocalization in the NFs that were previously prepared using Nile Red (see section 2.1.1) and FITC (see section 2.2) were analyzed using an LSM710 NLO (Carl Zeiss, Germany) CLSM instrument. The NE-loaded NF (hereafter NF-NE) and NE samples were placed on glass slides and their fluorescence was observed after excitation with Ar laser at 488 and 514 nm for the NE-NF samples treated with FITC (green signal) and Nile red (red signal), respectively, and at 514 nm with 2% laser capacity for NE. RGB images with a resolution of 1024 × 1024 pixels were captured using a Plan-Apochromat 63×/1.40 oil objective, and the images were processed using the ZEN software (Carl Zeiss, Germany). The overlap coefficient (r) was defined as [12]:

$$r = \frac{\sum_i Ch1_i \cdot Ch_{2i}}{\sqrt{[\sum_i (Ch1_i)^2 \cdot \sum_i (Ch2_i)^2]}}, \quad (1)$$

where *Ch*1 (channel 1) and *Ch*2 (channel 2) were assigned to FITC and red Nile, respectively. Two split overlap coefficients were used because the intensities of the red and green signals, M_1 and M_2, respectively, were independent of each other:

$$M_1 = \frac{\sum_i Ch1_{i,coloc}}{\sum_i Ch1_{i,total}} \quad (2)$$

and

$$M_2 = \frac{\sum_i Ch2_{i,coloc}}{\sum_i Ch2_{i,total}}, \quad (3)$$

where M_1 and M_2 are the sums of the intensities of the colocalized pixels for *Ch*1 and *Ch*2, respectively, reported to the overall sums of the pixel intensities above the threshold for each channel. All these coefficients (i.e., r, M_1, and M_2) ranged from 0 (no colocalization) to 1(complete colocalization) [12].

2.4. Nanomechanical properties

The surfaces of the NF-NE samples were indented using a DNP-10A (Bruker, USA) cantilever (silicon nitride-tip radius of 20 nm and half angle of 18°) and were subsequently analyzed using a Bio-AFM (Bioscope-Catalyst, Bruker, USA) atomic force microscopy (AFM) instrument (Figs. 2b-e). The cantilever spring-constant (k) was 0.35 N m^{-1} and the average deflection

sensitivity of the cantilever was 19.7 ± 0.9 nm/V. The indentation regions were selected using an Axio Observer.Z1 (Carl Zeiss, Germany) optical microscope. Indentations were made in the central area of the NF samples and the average indented depth was ~25 nm.

Force vs. indentation distance curves were collected using the point-and-shoot mode. The Nanoscope Analysis (version 1.50, Bruker, USA) software and Hertz model (Eq. 4) were used to calculate the elastic moduli (*E*, the resistance of materials to elastic (recoverable) deformation) of the samples [13], which were estimated assuming that the Poisson ratio (ν) was 0.3 [5].

$$F = \frac{2}{\mu}\frac{E}{(1-\nu^2)}\delta^2 \tan\alpha, \qquad (4)$$

where *F* is the force (nN), δ is the indentation distance (nm), and α the half angle of the tip (°). To determine $\Delta\gamma$, the Tabor number (μ) was calculated, and the Johnson–Roberts–Kendall (JRK) or Derjaguin–Muller–Toporov models were used, as follows:

$$\mu = \left(\frac{R\Delta\gamma^2}{E_r^2 z_0^3}\right)^{1/3}, \qquad (5)$$

where *R* is the radius of tip, E_r can be calculated using Eq. (6), and z_0 is the equilibrium separation of the sample (0.1 nm [14]);

$$E_r = \frac{E}{(1-\nu^2)}. \qquad (6)$$

The JRK model can be used when $\mu > 5$, and $\mu > 686$ for all NF-NE samples in this study. $\Delta\gamma$ was calculated from the measured pull-off forces (unloading curves) using Eq. (7).

$$\Delta\gamma = -\frac{2}{3}\frac{F_{adh}}{\pi R}, \qquad (7)$$

where F_{adh} is the maximum adhesion force, which was determined from the unloading curve [15]. Approximately 70 nanoindentations were processed to calculate *E* and approximately 60 to determine F_{adh} and $\Delta\gamma$.

2.5. Statistical analysis

The Minitab 16® (Minitab Inc., State College Chicago, USA) statistical software was used to perform ANOVA and the Tukey analysis of the ζ values of the NEs, oil distribution, protein structure, colocalization, and nanomechanical properties of the obtained NFs-based films. ANOVA and the Dunnett analysis were performed to compare the control (NE-free NFs) with the samples (NE-loaded NFs).

3. Results and discussion

3.1. NE characterization

The droplet size is a relevant factor for NEs because it directly affects their physical characteristics and stability, and hence, the *ADSs*, *PdIs*, and size droplet distributions of all HOPO NEs in this study were determined (Fig. 1). The *ADS* increased linearly with the HOPO concentration, and the *ADSs* of the NE5, NE10, NE15, and NE20 samples were 183 ± 2, 217 ± 1, 281 ± 1, and 354 ± 1 nm, respectively. This behavior has been previously reported by Ricaurte et al. (2018). At higher oil concentrations, the number of droplets in the aqueous phase increased and the probability of the oil droplets to escape to the high-shear zone during microfluidization and generate a broad droplet size distribution was higher [17]. This could explain the increase in *PdIs* with the HOPO concentration, and the *PdIs* of the NE5, NE10, NE15, and NE20 samples were 0.15, 0.20, 0.33, and 0.44, respectively. Furthermore, the *PdI* determines the amplitude of the droplet size distribution. The NEs with *PdIs* lower than 0.33 presented monodisperse droplet distribution (Figs. 1a and b) and good physical stability [18]. Conversely, broad oil droplet size distributions were observed for the NEs with *PdIs* of 0.33 or higher (Figs. 1c and d).

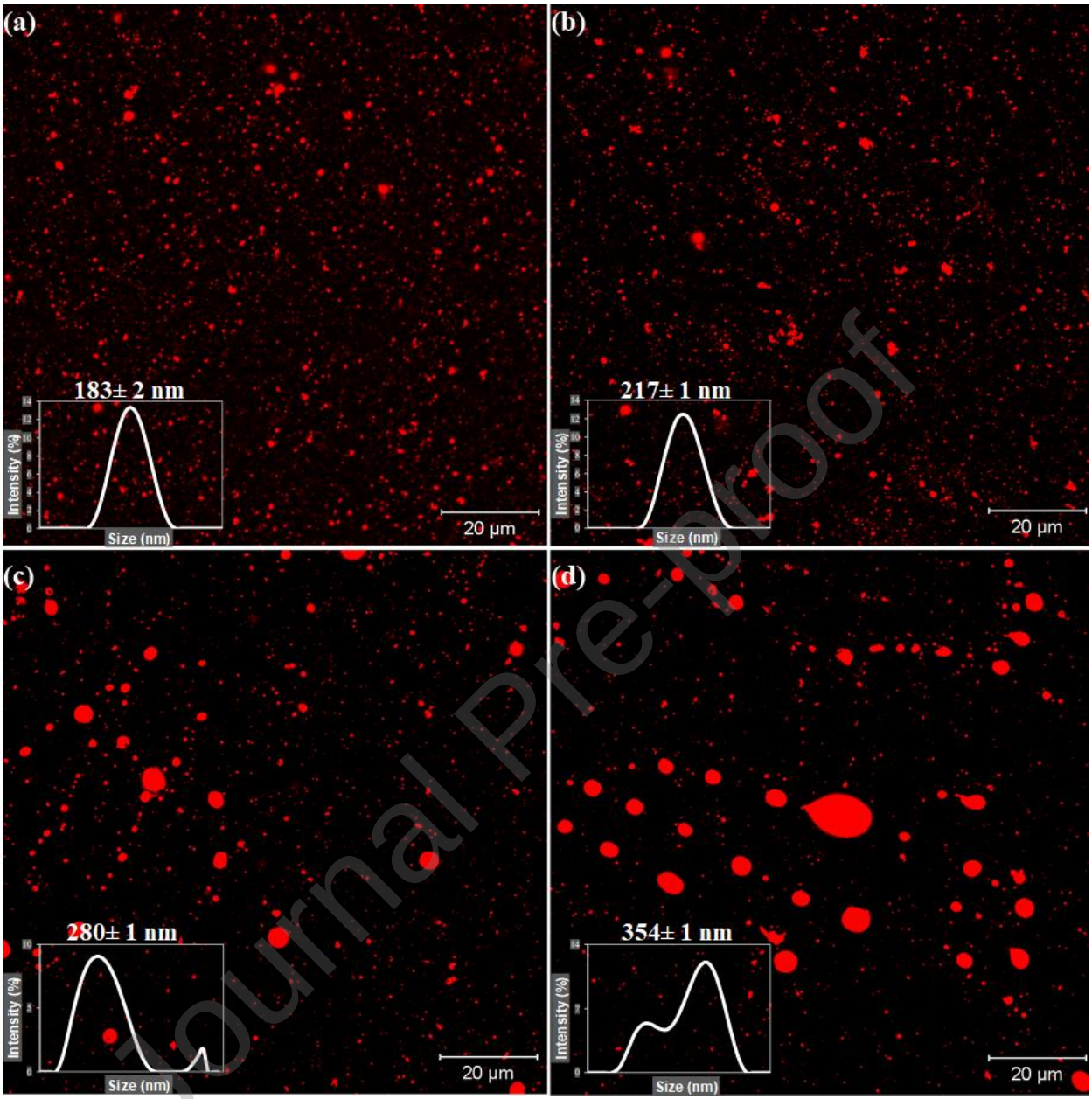

Figure 1. CLSM micrographs of NEs with **(a)** 5% w/w, **(b)** 10% w/w, **(c)** 15% w/w, and **(d)** 20% w/w HOPO concentration. The graphics on the lower left side represent the droplet size distribution related with polydispersity index (PdI).

The ζ values of NE5, NE10, NE15, and NE20 were determined to be −39 ± 1, −32 ± 1, −31 ± 1, and −31 ± 1 mV, respectively. According to the ANOVA and Tukey analysis, ζ of NE5 was significantly different ($p < 0.05$) than those of NE10, NE15, and NE20. However, the ζ values of all NEs were more negative than −30 mV, which indicated that the NEs were highly stable owing to the predominance of the repulsive forces in their structure [19]. In addition, higher ζ

values can be obtained when the system is over-processed or over-energized caused by new droplets form via re-coalescence [17].

3.2. NF morphology and diameter

Several researches have encapsulated emulsions into NFs (García-Moreno et al. 2016; Gómez-Mascaraque et al. 2017). In particular, Ricaurte et al. (2020) loaded HOPO NE and macroemulsions into NFs and demonstrated that the emulsion type did not significantly affect D_f. In this study, the effect of the HOPO concentration of the NE incorporated into gelatin-based NFs was studied.

As presented in Table 1S, D_f ranged from 49 to 130 nm, which indicated that the NFs were nanoscale-sized (Katouzian and Jafari, 2016). Furthermore, the D_f values of NF-NE0 and NF-NE20 were statistically different ($p < 0.05$), and the D_f value of NF-NE0 was lower than that of NF-NE-20. This was attributed to the contribution of solid concentrations of the NEs, i.e., whey protein and HOPO, which became part of the wall material network, and subsequently formed NFs. Zhang et al. (2019) reported that higher biopolymer concentrations produced NFs with larger D_f values. Moreover, the D_f values of NF-NE5, NF-NE10, and NF-NE15 were intermediate between those of NF-NE0 and NF-NE20.

The scanning electron microscopy (SEM) images of the NF-NE samples revealed the presence of few defects in their morphology (Fig. 2a). Some beads can be observed in Fig. 2a, and their presence was attributed to the partial evaporation of the solvent. Similar effects were obtained when corn oil emulsions were incorporated into gelatin-based NFs. The oil was mainly encapsulated inside the beads whose average diameter reached approximately 510 nm, while D_f was 125 nm (Zhang et al., 2019). The *ADS* of the corn oil emulsion-loaded NFs ranged from 5.77 to 9.78 μm; in contrast, the maximum *ADS* of the HOPO NEs was 353.5 nm (see section 3.1); NEs facilitated the dispersion of oil droplets inside the NF matrix, because the beads showed a smaller size. Therefore, it was confirmed that electrospinning efficiently evaporated the solvent and generated nanoscale-sized fibers. The SEM image of the NF revealed that the surface was smooth and uniform and presented no dots (dots with different contrasts can be observed for low-soluble compounds). This indicated that the gelatin solution and HOPO NEs formed homogeneous combinations (Fig. 2a).

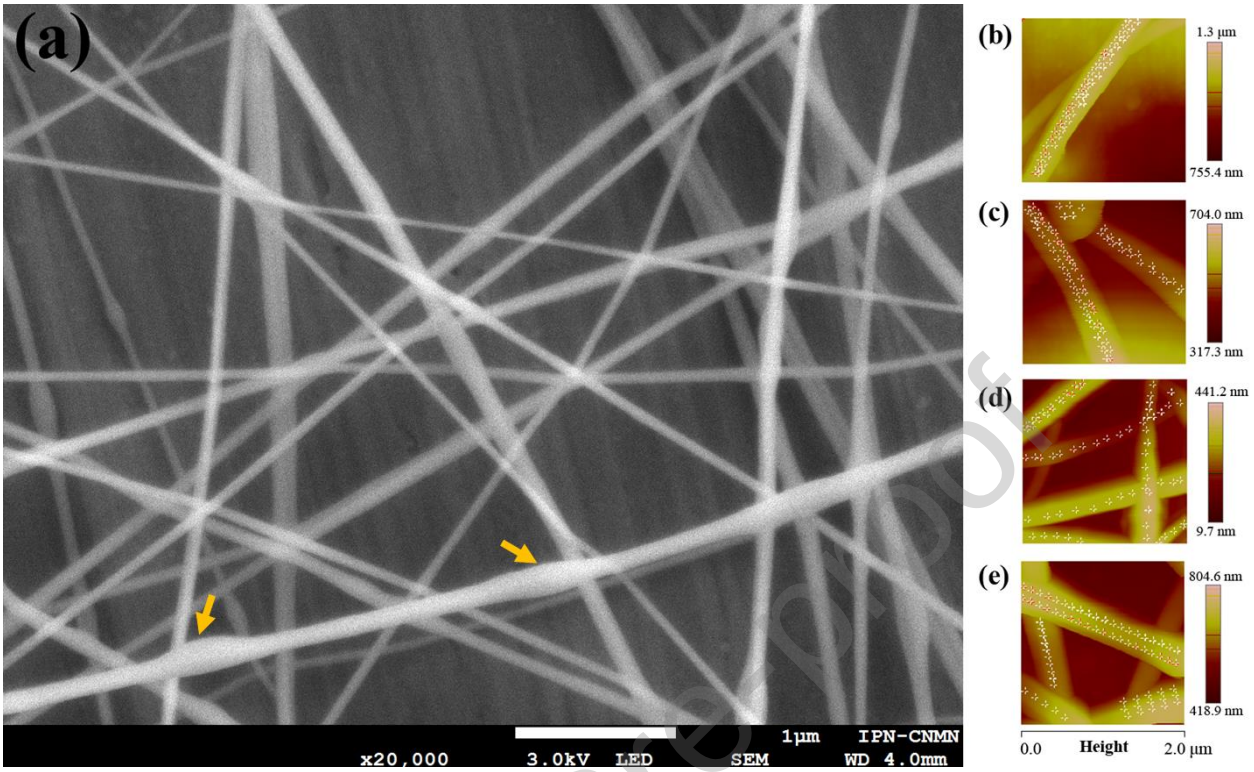

Figure 2. Representative SEM micrograph of NF-NE20 indicating beads with arrows **(a)** and AFM images of NFs loaded with NE: **(b)** NF-NE5, **(c)** NF-NE10, **(d)** NF-NE15, and **(e)** NF-NE20. The indentations are indicated in AFM images through plus symbols.

3.3. Protein integrity

FTIR is a fast, non-destructive, and simple analysis method that can be used to analyze the conformation of proteins using dry, wet, or deuterated samples. Proteins consist of repeating units, i.e., amides A, B, and I-VII, which generate characteristic IR bands, [9], and the bands of amides I, II, and III are the most relevant (Fig. 1S). The spectral region of amide I in the wavenumber range of 1600-1700 cm^{-1} is the most sensitive to the secondary structural components of proteins and corresponds mainly to the stretching of the C=O bonds. In addition, the peaks at 1235 and at 1450 cm^{-1} in the spectral regions of amides II and III are used to describe the triple helical structure of proteins (Sizeland et al. 2018). Moreover, CN stretching and NH bending combinations (out-of-phase and in-phase, respectively) are typically observed in the spectral regions of amides II and III.

The structural confirmation and protein integrity of the NFs in this study were determined using the spectral regions of amides I and III. Figure 3a illustrates the four peaks used to distinguish the secondary structures from the protein in the NFs as follows: the peaks at 1690 and 1670 cm^{-1} were ascribed to the β-turns, the peak at 1653 cm^{-1} was associated with the α-helix structure, the peak of the β-sheets was observed at 1637 cm^{-1}, and the peak at 1648 cm^{-1} was attributed to the random coil [25]. These band areas were quantified and expressed in percentages, as illustrated in Fig. 3b. The secondary structures of the NE-free NFs (control sample) were compared with those of the NF-NE samples using ANOVA and the Dunnett analysis, and the results indicated that they were not statistically different ($p > 0.05$). However, the fraction of β-sheet structure decreased as the HOPO concentration of the NEs increased (Fig. 3b). In addition, more compact structures were formed between gelatin and the HOPO NEs via hydrogen bonding [26].

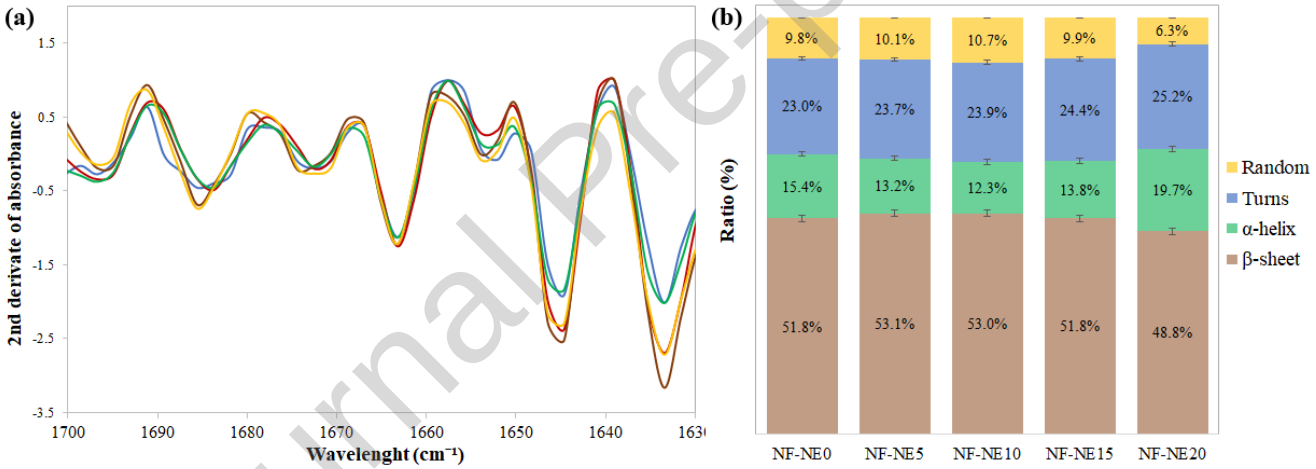

Figure 3. Second derivate FTIR spectra **(a)** of NFs loaded with NE: (▬) NF-NE0, (▬) NF-NE5, (▬) NF-NE10, (▬) NF-NE15, and (▬) NF-NE20.

The helical structure of the control was compared with those of the NF-NE samples, and the results are summarized in Table 2S. The absence of the HOPO NE did not significantly affect the triple helical structure of the NFs ($p = 0.95$). For the control sample, the 1235 cm^{-1}:1450 cm^{-1} peak absorption ratio was greater than 1, which indicated that triple helices were present in its structure (Sizeland et al. 2018). For all NF-NE samples, the 1235 cm^{-1}:1450 cm^{-1} peak absorbance ratios were approximately 0.8 and were ascribed to bromelain causing the partial hydrolysis of gelatin. The 1235 cm^{-1}:1450 cm^{-1} peak absorption ratios of the electrospun NF produced by Sizeland et al. (2018) using porcine gelatin and collagen were lower than 0.75. They

concluded that the NFs did not contain triple helical structures because electrospinning caused molecular conformation changes. However, our results did not indicate an attributable relationship caused by electrospinning, but to a partial denaturation of gelatin. In addition, it was demonstrated that oil droplets were integrated in the protein network and affected its properties, such as the crystallinity and thermal stability [2]. However, in this study, stable nanostructures were obtained between the HOPO NEs and gelatin, and hence, no structural conformational changes were associated with the NF formulations.

The linear structure of synthetic polymers must be reproduced during electrospinning to ensure the stretching of the biopolymer and formation of the fibers [27]. The α-helix, β-sheet, and helical structures are the most important conformations for gelatin. The α-helix structure is a rod-like structure that is formed via hydrogen bonding between the CO groups of amino acids and NH groups located four residues ahead in the amino acid sequence of the protein [28]. This pattern generates a helical structure similar to a curled ribbon, which facilitates the formation of stiff fiber bundles. The β-sheet is formed by the polypeptide chain termed the β strand, which is almost fully extended (Berg et al. 2002). This structure is particularly important for fatty acids binding and can contribute to the formation of oil-loaded fibers.

3.4. Oil distribution inside the NF matrix

FTIR is a versatile technique that has been used for oil authentication (Rohman et al. 2014), oil adulteration [29], lipid oxidation measurements (Daoud et al. 2019), and confirming the encapsulation of oils (Sathasivam et al. 2018). Two characteristic bands of HOPO and one of gelatin are highlighted in the FTIR spectra of all NE-NFs (Fig. 1S-b). The strong band at 1745 cm^{-1} was ascribed to the stretching vibrations of the carbonyl group of the triglyceride esters (–C=O) and the band at 2855 cm^{-1} was related to the asymmetric and symmetric stretching vibrations of the $–CH_3$ groups (Daoud et al. 2019). The strong band at 2930 cm^{-1} was associated with the asymmetric and symmetric stretching vibrations of the $–CH_2–$ groups of gelatin. This band has been previously observed in the FTIR spectra of gelatin-based NFs (Deng et al. 2020), and therefore, it was used as a reference band to determine the presence of HOPO in the analyzed samples.

The band at 1745 cm^{-1} presented two statistical groups because the HOPO concentrations of the NEs loaded into the gelatin-based NFs were statistically significant ($p < 0.05$) (Table 1). The integration areas of the NF-NE5 and NF-NE10 samples were lower than those of the NF-NE15 and NF-NE20 samples owing to the lower HOPO concentrations of the NEs used to fabricate the NF-NE5 and NF-NE10 samples. Furthermore, the intensity of the bands ascribed to the –C=O vibrations increased with increasing HOPO concentration. The 1745 cm^{-1}:2930 cm^{-1} peak absorption ratios of the NF-NE samples were similar, which demonstrated the proportional increase in the intensities of the –C=O and $–CH_2–$ vibration bands with the HOPO concentration. The 2855 cm^{-1} band, which was ascribed to the vibration of the $–CH_2–$ groups, was used to determine the effect of the HOPO concentration on NFs, and the intensity of the band increased as the HOPO concentration increased. Three statistically different groups were obtained ($p < 0.05$) for this band, as illustrated in Table 1. The 2855 cm^{-1}:2930 cm^{-1} peak absorption ratio increased as the HOPO concentration increased, i.e., the $–CH_3$ vibrations were stronger than the $–CH_2–$ vibrations owing to the surface exposition of oil, which confirmed the different HOPO NE loads inside the NF matrices.

Table 1. Absorption ratios regarding oil-protein presence of NFs loaded with several HOPO concentrations in NEs

Sample	**Average integration area**			**1745 cm^{-1}:2930 cm^{-1}**	**2855 cm^{-1}:2930 cm^{-1}**
	~2930 cm^{-1}	**~2855 cm^{-1}**	**~1745 cm^{-1}**	**ratio**	**ratio**
NF-NE0	0.66 ± 0.3^{a}	-	-	-	-
NF-NE5	0.91 ± 0.5^{a}	0.03 ± 0.01^{a}	0.01 ± 0.00^{a}	0.01^{a}	0.04^{a}
NF-NE10	2.21 ± 1.1^{b}	0.12 ± 0.02^{b}	0.09 ± 0.01^{ab}	0.04^{ab}	0.05^{ab}
NF-NE15	2.35 ± 1.2^{bc}	0.15 ± 0.04^{bc}	0.12 ± 0.06^{b}	0.05^{b}	0.06^{bc}
NF-NE20	2.60 ± 1.3^{c}	0.20 ± 0.02^{c}	0.15 ± 0.03^{b}	0.06^{b}	0.08^{c}

Different letters mean statistical differences ($p < 0.05$) in NF loaded with HOPO concentration into NEs for each band and ratios: a, b and c were used

CLSM is a powerful analysis tool that allows to obtain dual-color images for the simultaneous detection of two fluorochromes in the same sample. These types of images are particularly useful when analyzing colocalization, because they allow to determine whether molecules are located in the same spot [32]. CLSM is particularly useful for biology applications, including the

identification of the location of specific compounds in cells [33] or the study of cellular receptor trafficking and endocytosis [34,35]. In this study, CLSM was used to complement the FTIR data and determine the degree of colocalization between HOPO and gelatin. The combined information helped us to elucidate the distribution of the HOPO droplets in the NF matrix, and hence, CLSM added a qualitative-quantitative perspective.

The weighted colocalization coefficient (M_i) can be determined for two signals, considering the intensity value of summed pixels (M_1 and M_2 are independent on the intensities of the red and green signals, respectively) [12]. Table 2 presents the M_1 and M_2 values, where the protein was assigned to channel 1 (FITC, green signal) and HOPO to channel 2 (Nile red, red signal). The type of sample i.e., electrospun solution or NF, significantly affected ($p < 0.05$) M_1. Gelatin was more dispersed in the electrospun solutions than in the NF matrices owing to the reorganization it was subjected to during electrospinning. When the electric force (associated with the provided high voltage) was equal to the surface tension of the electrospun solution, a Taylor cone was formed and droplets at the syringe tip were stretched on a metal collector. The high fiber deposition rate during electrospinning generates a change from disordered to oriented and organized proteins. The fluorescence of the HOPO droplets (M_2) was the same for both the electrospun solutions and NFs i.e., the sum of total oil droplet fluorescence was the same before and after electrospinning, presenting then no significant effect ($p = 0.35$). As illustrated in Fig. 2S, the fluorescence of the NE droplets in the electrospun solutions was stronger than that in the NFs; however, the total fluorescence for the two types of samples was the same. Furthermore, the intensity of the red signal increased with the increase in HOPO concentration (Fig. 2S-b).

Table 2. Colocalization coefficients for electrospun solutions and NFs with different HOPO concentration in NE

Sample type	**Sample**	***M₁***	***M₂***	***r***
	NE5	0.07± 0.08[a]	0.5± 0.2[a]	0.67± 0.02[a]
Electrospun	NE10	0.16± 0.02[a]	0.5± 0.1[a]	0.69± 0.02[a]
solutions[1]	NE15	0.16± 0.04[a]	0.3± 0.1[a]	0.68± 0.03[a]
	NE20	0.11± 0.04[a]	0.4± 0.1[a]	0.64± 0.01[a]

Nanofibers	NF-NE5	0.3± 0.1[b]	0.5± 0.1[a]	0.63± 0.05[a]
	NF-NE10	0.31± 0.07[b]	0.4± 0.2[a]	0.63± 0.01[a]
	NF-NE15	0.36± 0.05[b]	0.3± 0.2[a]	0.67± 0.03[a]
	NF-NE20	0.24± 0.02[b]	0.2± 0.03[a]	0.58± 0.03[a]

[1]Electrospun solutions were formed by mechanical blend of gelatin solution and NE

Sample types were compared for each variable. Different letters mean statistical differences ($p < 0.05$): a and b were used.

Different labelling, fluorochromes, or photo-bleaching have no effect on *r* because no sensitivity in signal intensities between components of an image. The type of sample did not affect *r* significantly ($p = 0.09$) (Table 2), and the colocalization of the protein and oil was similar for both types of samples. These results were unexpected because our hypothesis was that *r* of the NFs would be higher than that of the electrospun solutions, for which the protein and HOPO NEs were more organized. However, the ratio of pixels for the two channels could explain these results; lower M_1 values and higher M_2 values for electrospun solutions had better match in ratio between the green and red pixels, increasing *r*, in contrast green and red pixels from NF had less coincidence. The presence of HOPO NE along the NFs was observed, which confirmed a high dispersion and the presence of oil in the samples. This characteristic could be associated with the efficient and controlled release of HOPO from the NF matrix for food applications. A survey of the literature revealed that this is the first study to use colocalization for the characterization of NFs.

3.5. Nanomechanical properties

AFM was used to evaluate the nanomechanical properties of the analyzed films. Nanoindentation is an AFM-based technique that can be used to determine properties, such as *E*, F_{adh}, $\Delta\gamma$, and hardness, using cantilevers [5,36,37]. Cantilevers are indenters with spherical or pyramidal tips. The deflection of the tip is ascribed to the repulsion or attraction between the tip and sample surface during indentation. The applied force can be measured using the reflection of a laser beam focused on the backside of the cantilever onto a photodiode [37] and *k*. A wide range of materials, from hard compounds to soft polymers, and a variety of nanoscale structures can be analyzed via nanoindentation, e.g., deposited NF on a flat collector.

In this study, nanoindentation was used to analyze the nanomechanical properties of the NF-NE samples (Figs. 2b-e). To determine the proper model for the experimental conditions, μ which represents 'the ratio of the elastic displacement of the surfaces at the point of pull-off to the effective range of surface forces characterized by z_0 (equilibrium separation)', was calculated using Eq. (5) [38]. Because μ was higher than 686 for all the NF samples in this study, the JRK adhesion model was used to analyze the unloading curves of the force vs. indent plots. In addition, the E, E_r, F_{adh}, and $\Delta\gamma$ values of all samples were determined, and the results are summarized in Table 3.

Table 3. Nanomechanical properties of NFs loaded with different HOPO concentrations into NEs

Sample	*Nanomechanical properties*[1]			
	***E* (Mpa)**	**E_r (Mpa)**	**F_{adh} (nN)**	**$\Delta\gamma$ (J/m^2)**
NF-NE5	53± 29^{a}	58± 32^{a}	16± 4^{a}	69± 15^{a}
NF-NE10	53± 31^{a}	58± 34^{a}	14± 5^{b}	61± 20^{b}
NF-NE15	63± 28^{a}	69± 30^{a}	15± 7^{ab}	64± 29^{ab}
NF-NE20	63± 25^{a}	69± 28^{a}	18± 9^{a}	74± 38^{a}

[1]E: elastic modulus, E_r: reduced modulus, F_{adh}: Maximum adhesion force and $\Delta\gamma$: work of adhesion

As revealed by the data in Table 3, the different HOPO concentrations in NE loaded in NFs did not significantly affect ($p < 0.05$) E or E_r. The histograms in Fig.4 illustrate that at higher HOPO concentrations in NF, the frequencies achieved higher classes. This behavior was in good agreement with the size of the oil droplets that were loaded into the NF matrix. Low E values are associated with floppy and stretchable materials [39], then smaller oil droplet size (lower HOPO concentration), decreased the elasticity of NF. Furthermore, E depends on the material constitutive relations (Umer et al. 2018). These mechanical properties of the analyzed samples confirmed the homogeneity and synergism between the gelatin solution and NEs; moreover, the high stability of the samples was confirmed using the FTIR spectroscopy, CLSM, and AFM

results. Zhang et al. (2011) reported that the *E* of cholesteryl-succinyl silane (CSS) NFs ranged from 55.3 to 70.8 MPa and ascribed the difference of *E* values to the altering of hydrolysis and polymerization of CSS molecules. Furthermore, the total recovery of NF after indentations was observed (data not shown), i.e., the NFs presented no structural variations (no notches or indentation marks).

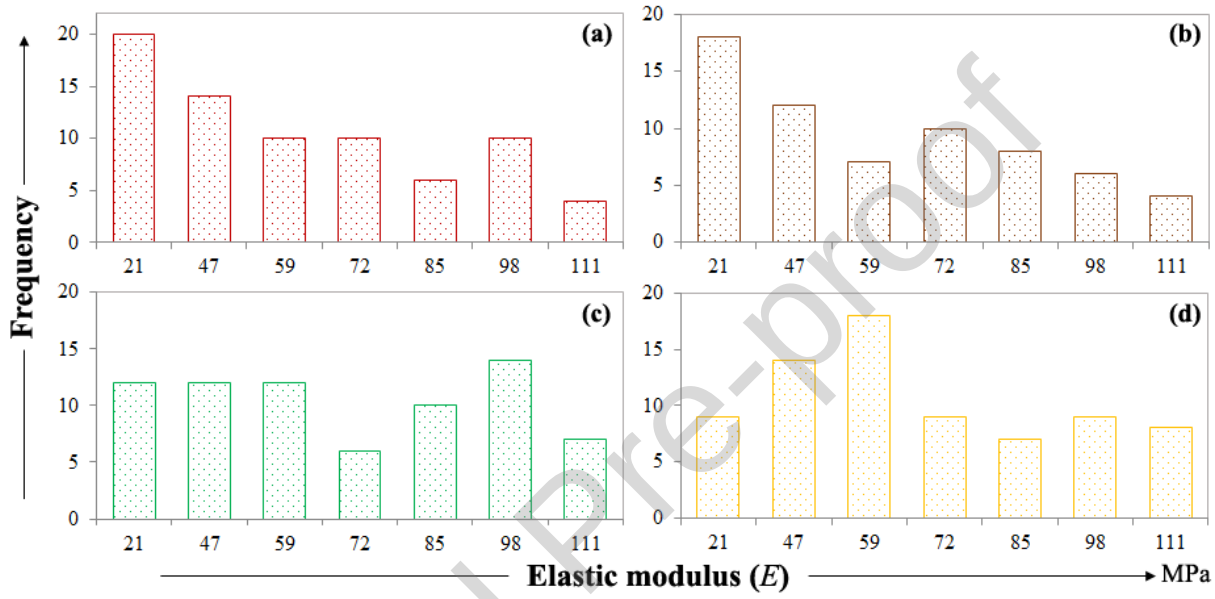

Figure 4. The frequency histogram of elastic modulus of NFs loaded with NE: **(a)** NF-NE5, **(b)** NF-NE10, **(c)** NF-NE15, and **(d)** NF-NE20.

The F_{adh} and $\Delta\gamma$ between the AFM probe and surface of the NFs were obtained (Table 3) and a prominent pull-off peak was observed in the unloading curves of all samples; in addition, both properties were statistically significant ($p < 0.05$). The F_{adh} and $\Delta\gamma$ of the NF-NE5 and NF-NE20 samples were higher than those of the NF-NE10 and NF-NE15 samples. The HOPO NE in the NF matrix could generate a sticky surface, doing that pull-off forces increased. Likewise, the synergy between compounds which could present a better chemical interaction, increasing interfacial interactions between the cantilever tip and NFs [41]. Despite these adhesion properties, the unloading curves revealed that the indentation depth did not increase, which indicated that plastic deformation did not increase the crystal packing density and directional deformation did not induce a more compact arrangement of the protein chains [5].

These nanomechanical properties of NF matrix are relevant for food packaging due to this is a potential and significant contribution to that application. AFM is typically used to analyze the morphology of surfaces; however, AFM-based techniques, could be used for structure identification and also to determine the physical, thermal, magnetic, or electric properties of materials [42].

4. Conclusions

HOPO NEs were successfully encapsulated into gelatin-based NFs. FTIR spectroscopy was used as a fast and reliable tool to qualitatively analyze the structure of gelatin and HOPO in the NF-NE samples. Gelatin preserved its helical structure, which is required for electrospinning, and HOPO loading was determined inside the NF matrix using characteristic bands from FTIR spectra. CLSM was used for colocalization analysis, and the results allowed us to establish the high coincidence frequency and homogeneous distribution of gelatin and HOPO in the NFs. The nanomechanical properties of the biofilms indicated that the NFs presented high elasticity and recovery after deformation; in addition, higher oil concentrations led to the decrease in the *E* of the samples. Adhesion forces were also observed due to the surface oil. These NF-based films could be used as edible packaging, and their nutritional value would be attributed to the materials used to fabricate them. Moreover, high HOPO NE loads could add functional characteristics, such as antioxidant activity and high thermal stability to these biofilms.

CRediT authorship contribution statement

Leidy Ricaurte: Conceptualization, Methodology, Investigation, Writing - original draft, Project administration. ***María de Jesus Perea-Flores:*** Methodology, Investigation, Writing - review & editing. ***Juan Vicente Méndez-Méndez:*** Methodology, Investigation, Writing - review & editing. ***Patricio Román Santagapita:*** Formal analysis, Writing - review & editing. ***Maria Ximena Quintanilla-Carvajal:*** Conceptualization, Methodology, Resources, Writing - review & editing, Funding acquisition.

Declaration of Competing Interest

☒ The authors declare that they have no known competing financial interests or personal relationships that could have appeared to influence the work reported in this paper.

☐The authors declare the following financial interests/personal relationships which may be considered as potential competing interests:

Acknowledgments

The authors would like to thank the Universidad de La Sabana for financing this research by funding project ING-170-2016. We would also like to acknowledge Cenipalma Colombia for kindly supplying the high-oleic palm oil used in this study and to Alexandra Mondragón Serna, leader of Cenipalma's Health and Nutrition project. Leidy Ricaurte acknowledges COLCIENCIAS for awarding her PhD scholarship (grant number 727-2015).

Declaration of Competing Interest

The authors declare that they have no known competing financial interests or personal relationships that could have appeared to influence the work reported in this paper.

References

[1] C. Liu, J. Huang, X. Zheng, S. Liu, K. Lu, K. Tang, J. Liu, Heat sealable soluble soybean polysaccharide/gelatin blend edible films for food packaging applications, Food Packag. Shelf Life. 24 (2020) 100485. https://doi.org/https://doi.org/10.1016/j.fpsl.2020.100485.

[2] L. Ricaurte, P.R. Santagapita, L.E. Díaz, M.X. Quintanilla-Carvajal, Edible gelatin-based nanofibres loaded with oil encapsulating high-oleic palm oil emulsions, Colloids Surfaces A Physicochem. Eng. Asp. 595 (2020) 124673. https://doi.org/10.1016/j.colsurfa.2020.124673.

[3] M. Nieuwland, P. Geerdink, P. Brier, P. van den Eijnden, J.T.M.M. Henket, M.L.P. Langelaan, N. Stroeks, H.C. van Deventer, A.H. Martin, Reprint of "Food-grade electrospinning of proteins," Innov. Food Sci. Emerg. Technol. 24 (2014) 138–144. https://doi.org/10.1016/j.ifset.2014.07.006.

[4] K.H. Sizeland, K.A. Hofman, I.C. Hallett, D.E. Martin, J. Potgieter, N.M. Kirby, A. Hawley, S.T. Mudie, T.M. Ryan, R.G. Haverkamp, M.H. Cumming, Nanostructure of electrospun collagen: Do electrospun collagen fibers form native structures?, Materialia. 3 (2018) 90–96. https://doi.org/10.1016/j.mtla.2018.10.001.

[5] J. Shao, Y. Wang, X. Chen, X. Hu, C. Du, Nanomechanical properties of poly(l-lactide) nanofibers after deformation, Colloids Surfaces B Biointerfaces. 120 (2014) 97–101. https://doi.org/10.1016/j.colsurfb.2014.05.021.

[6] L. Ricaurte, M.D.J. Perea-Flores, A. Martinez, M.X. Quintanilla-Carvajal, Production of high-oleic palm oil nanoemulsions by high-shear homogenization (microfluidization), Innov. Food Sci. Emerg. Technol. 35 (2016) 75–85. https://doi.org/10.1016/j.ifset.2016.04.004.

[7] L. Ricaurte, E. Tello-Camacho, M.X. Quintanilla-Carvajal, Hydrolysed Gelatin-Derived, Solvent-Free, Electrospun Nanofibres for Edible Applications: Physical, Chemical and Thermal Behaviour, Food Biophys. (2019). https://doi.org/10.1007/s11483-019-09608-9.

[8] D.F. Roa-Acosta, J.E. Bravo-Gómez, M.A. García-Parra, R. Rodríguez-Herrera, J.F.

Solanilla-Duque, Hyper-protein quinoa flour (Chenopodium Quinoa Wild): Monitoring and study of structural and rheological properties, Lwt. 121 (2020) 108952. https://doi.org/10.1016/j.lwt.2019.108952.

[9] J. Kong, S. Yu, Fourier transform infrared spectroscopic analysis of protein secondary structures, Acta Biochim. Biophys. Sin. (Shanghai). 39 (2007) 549–559. https://doi.org/10.1111/j.1745-7270.2007.00320.x.

[10] A. Rohman, S. Riyanto, A.M. Sasi, F.M. Yusof, The use of FTIR spectroscopy in combination with chemometrics for the authentication of red fruit (Pandanus conoideus Lam) oil from sunflower and palm oils, Food Biosci. 7 (2014) 64–70. https://doi.org/10.1016/j.fbio.2014.05.007.

[11] M.A. Poiana, E. Alexa, M.F. Munteanu, R. Gligor, D. Moigradean, C. Mateescu, Use of ATR-FTIR spectroscopy to detect the changes in extra virgin olive oil by adulteration with soybean oil and high temperature heat treatment, Open Chem. 13 (2015) 689–698. https://doi.org/10.1515/chem-2015-0110.

[12] E.M.M. Manders, F.J. Verbeek, J.A. Aten, Measurement of co-localization of objects in dual-colour confocal images, J. Microsc. 169 (1993) 375–382. https://doi.org/10.1111/j.1365-2818.1993.tb03313.x.

[13] G.N. Barrera, J. Méndez-Méndez, I. Arzate-Vázquez, G. Calderón-Domínguez, P.D. Ribotta, Nano- and micro-mechanical properties of wheat grain by atomic force microscopy (AFM) and nano-indentation (IIT) and their relationship with the mechanical properties evaluated by uniaxial compression test, J. Cereal Sci. 90 (2019) 102830. https://doi.org/10.1016/j.jcs.2019.102830.

[14] J. Umer, N. Morris, M. Leighton, R. Rahmani, S. Howell-Smith, R. Wild, H. Rahnejat, Asperity level tribological investigation of automotive bore material and coatings, Tribol. Int. 117 (2018) 131–140. https://doi.org/10.1016/j.triboint.2017.08.023.

[15] D.M. Ebenstein, Nano-JKR force curve method overcomes challenges of surface detection and adhesion for nanoindentation of a compliant polymer in air and water, J. Mater. Res. 26 (2011) 1026–1035. https://doi.org/10.1557/jmr.2011.42.

[16] L. Ricaurte, M. Hernández-Carrión, M. Moyano-Molano, A. Clavijo-Romero, M.X. Quintanilla-Carvajal, Physical, thermal and thermodynamical study of high oleic palm oil nanoemulsions, Food Chem. 256 (2018) 62–70. https://doi.org/10.1016/j.foodchem.2018.02.102.

[17] S.G. Sadeghpour, B. Dabir, Three-factor response surface optimization of nano-emulsion formation using a microfluidizer., J. Food Sci. Technol. 52 (2015) 2558–2571. https://doi.org/10.1007/s13197-014-1363-1.

[18] N. Riquelme, R.N. Zúñiga, C. Arancibia, Physical stability of nanoemulsions with emulsifier mixtures: Replacement of tween 80 with quillaja saponin, LWT. 111 (2019) 760–766. https://doi.org/https://doi.org/10.1016/j.lwt.2019.05.067.

[19] L. Salvia-Trujillo, A. Rojas-Graü, R. Soliva-Fortuny, O. Martín-Belloso, Physicochemical characterization and antimicrobial activity of food-grade emulsions and nanoemulsions incorporating essential oils, Food Hydrocoll. 43 (2015) 547–556. https://doi.org/http://dx.doi.org/10.1016/j.foodhyd.2014.07.012.

[20] L.G. Gómez-Mascaraque, R. Perez-Masiá, R. González-Barrio, M.J. Periago, A. López-Rubio, Potential of microencapsulation through emulsion-electrospraying to improve the bioaccesibility of β-carotene, Food Hydrocoll. 73 (2017) 1–12. https://doi.org/10.1016/j.foodhyd.2017.06.019.

[21] P.J. García-Moreno, K. Stephansen, J. Van Der Kruijs, A. Guadix, E.M. Guadix, I.S. Chronakis, C. Jacobsen, Encapsulation of fish oil in nanofibers by emulsion electrospinning: Physical characterization and oxidative stability, J. Food Eng. 183 (2016) 39–49. https://doi.org/10.1016/j.jfoodeng.2016.03.015.

[22] M.X. Quintanilla-Carvajal, B.H. Camacho-Díaz, L.S. Meraz-Torres, J.J. Chanona-Pérez, L. Alamilla-Beltrán, A. Jimenéz-Aparicio, G.F. Gutiérrez-López, Nanoencapsulation: A New Trend in Food Engineering Processing, Food Eng. Rev. 2 (2009) 39–50. https://doi.org/10.1007/s12393-009-9012-6.

[23] I. Katouzian, S.M. Jafari, Nano-encapsulation as a promising approach for targeted delivery and controlled release of vitamins, Trends Food Sci. Technol. 53 (2016) 34–48.

https://doi.org/10.1016/j.tifs.2016.05.002.

[24] C. Zhang, Y. Li, P. Wang, A. Zhang, F. Feng, H. Zhang, Electrospinning of bilayer emulsions: The role of gum Arabic as a coating layer in the gelatin-stabilized emulsions, Food Hydrocoll. 94 (2019) 38–47. https://doi.org/10.1016/j.foodhyd.2019.03.013.

[25] A. Dong, P. Huang, W.S. Caughey, Protein Secondary Structures in Water from Second-Derivative Amide I Infrared Spectra, Biochemistry. 29 (1990) 3303–3308. https://doi.org/10.1021/bi00465a022.

[26] L. Deng, Y. Li, A. Zhang, H. Zhang, Characterization and physical properties of electrospun gelatin nanofibrous films by incorporation of nano-hydroxyapatite, Food Hydrocoll. 103 (2020). https://doi.org/10.1016/j.foodhyd.2019.105640.

[27] L. Ricaurte, M.X. Quintanilla-Carvajal, Use of electrospinning technique to produce nanofibres for food industries: A perspective from regulations to characterisations, Trends Food Sci. Technol. 85 (2019) 92–106. https://doi.org/S0924224418303315.

[28] J. Berg, J. Tymoczko, L. Stryer, Section 3.3, Secondary Structure: Polypeptide Chains Can Fold Into Regular Structures Such as the Alpha Helix, the Beta Sheet, and Turns and Loops, in: Biochemistry, Fifth, W H Freeman, New york, 2002. https://www.ncbi.nlm.nih.gov/books/NBK22580/.

[29] Amit, R. Jamwal, S. Kumari, S. Kelly, A. Cannavan, D.K. Singh, Rapid detection of pure coconut oil adulteration with fried coconut oil using ATR-FTIR spectroscopy coupled with multivariate regression modelling, LWT. 125 (2020) 109250. https://doi.org/https://doi.org/10.1016/j.lwt.2020.109250.

[30] S. Daoud, E. Bou-maroun, L. Dujourdy, G. Waschatko, N. Billecke, P. Cayot, U.B. Franche-comté, A. Dijon, P.A.M.U.M.R. A, F.- Dijon, Fast and direct analysis of oxidation levels of oil-in-water emulsions using, Food Chem. 293 (2019) 307–314. https://doi.org/10.1016/j.foodchem.2019.05.005.

[31] T. Sathasivam, S. Muniyandy, L.H. Chuah, P. Janarthanan, Encapsulation of red palm oil in carboxymethyl sago cellulose beads by emulsification and vibration technology: Physicochemical characterization and in vitro digestion, J. Food Eng. 231 (2018) 10–21.

https://doi.org/10.1016/j.jfoodeng.2018.03.008.

[32] P.A. Fletcher, D.R.L. Scriven, M.N. Schulson, E.D.W. Moore, Multi-image colocalization and its statistical significance, Biophys. J. 99 (2010) 1996–2005. https://doi.org/10.1016/j.bpj.2010.07.006.

[33] E.I. Medina-Reyes, N.L. Delgado-Buenrostro, D.L. Leseman, A. Déciga-Alcaraz, R. He, E.R. Gremmer, P.H.B. Fokkens, J.O. Flores-Flores, F.R. Cassee, Y.I. Chirino, Differences in cytotoxicity of lung epithelial cells exposed to titanium dioxide nanofibers and nanoparticles: Comparison of air-liquid interface and submerged cell cultures, Toxicol. Vitr. 65 (2020) 104798. https://doi.org/https://doi.org/10.1016/j.tiv.2020.104798.

[34] R.N. Majzoub, C.-L. Chan, K.K. Ewert, B.F.B. Silva, K.S. Liang, C.R. Safinya, Fluorescence microscopy colocalization of lipid–nucleic acid nanoparticles with wildtype and mutant Rab5–GFP: A platform for investigating early endosomal events, Biochim. Biophys. Acta - Biomembr. 1848 (2015) 1308–1318. https://doi.org/https://doi.org/10.1016/j.bbamem.2015.03.001.

[35] J.A. Pike, I.B. Styles, J.Z. Rappoport, J.K. Heath, Quantifying receptor trafficking and colocalization with confocal microscopy, Methods. 115 (2017) 42–54. https://doi.org/10.1016/j.ymeth.2017.01.005.

[36] F. An, G. Zhong, Q. Zhu, Y. Huang, Y. Yang, S. Xie, Synthesis and mechanical properties characterization of multiferroic BiFeO3-CoFe2O4 composite nanofibers, Ceram. Int. 44 (2018) 11617–11621. https://doi.org/10.1016/j.ceramint.2018.03.235.

[37] B.R. Neugirg, S.R. Koebley, C. Schniepp, A. Fery, AFM-based mechanical characterization of single nanofibres, Nanoscale. 8 (2016) 8414–8426. https://doi.org/10.1039/c6nr00863a.

[38] K.L. Johnson, J.A. Greenwood, An Adhesion Map for the Contact of Elastic Spheres, J. Colloid Interface Sci. 192 (1997) 326–333. papers://ab3587e6-c7a5-4d48-999f-f9c49d47016a/Paper/p49.

[39] D.R.H. Jones, M.F. Ashby, Elastic Moduli, in: D.R.H. Jones, M.F.B.T.-E.M. 1 (Fifth E. Ashby (Eds.), Eng. Mater. An Introd. to Prop. Appl. Des., Butterworth-Heinemann, 2019:

pp. 31–47. https://doi.org/https://doi.org/10.1016/B978-0-08-102051-7.00003-8.

[40] J. Zhang, C. Cohn, W. Qiu, Z. Zha, Z. Dai, X. Wu, Atomic force microscopy of electrospun organic-inorganic lipid nanofibers, Appl. Phys. Lett. 99 (2011) 2012–2015. https://doi.org/10.1063/1.3635783.

[41] F. Carrillo, S. Gupta, M. Balooch, S.J. Marshall, G.W. Marshall, L. Pruitt, C.M. Puttlitz, Nanoindentation of polydimethylsiloxane elastomers: Effect of crosslinking, work of adhesion, and fluid environment on elastic modulus, J. Mater. Res. 20 (2005) 2820–2830. https://doi.org/10.1557/JMR.2005.0354.

[42] F. Marinello, A. La Storia, G. Mauriello, D. Passeri, Atomic Force microscopy techniques to investigate activated food packaging materials, Trends Food Sci. Technol. 87 (2019) 84–93. https://doi.org/10.1016/j.tifs.2018.05.028.

Graphical abstract

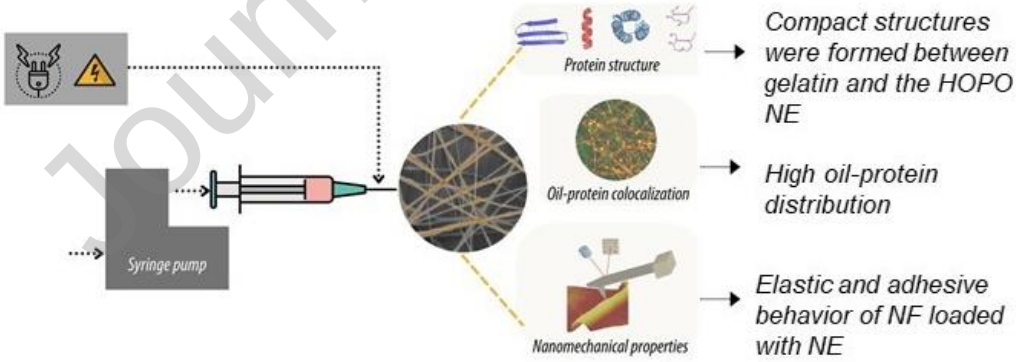

Highlights

- Smooth and defect-free NFs were loaded with HOPO NE via electrospinning
- Secondary and triple-helical protein structures of NFs were quantified by FTIR
- High oil-protein colocalization into NFs was obtained using CLSM
- Elastic modulus decreased at higher HOPO concentration in NE loaded into NFs
- Nanomechanical properties showed homogeneity and synergy of NEs and NFs compounds

Supplementary material

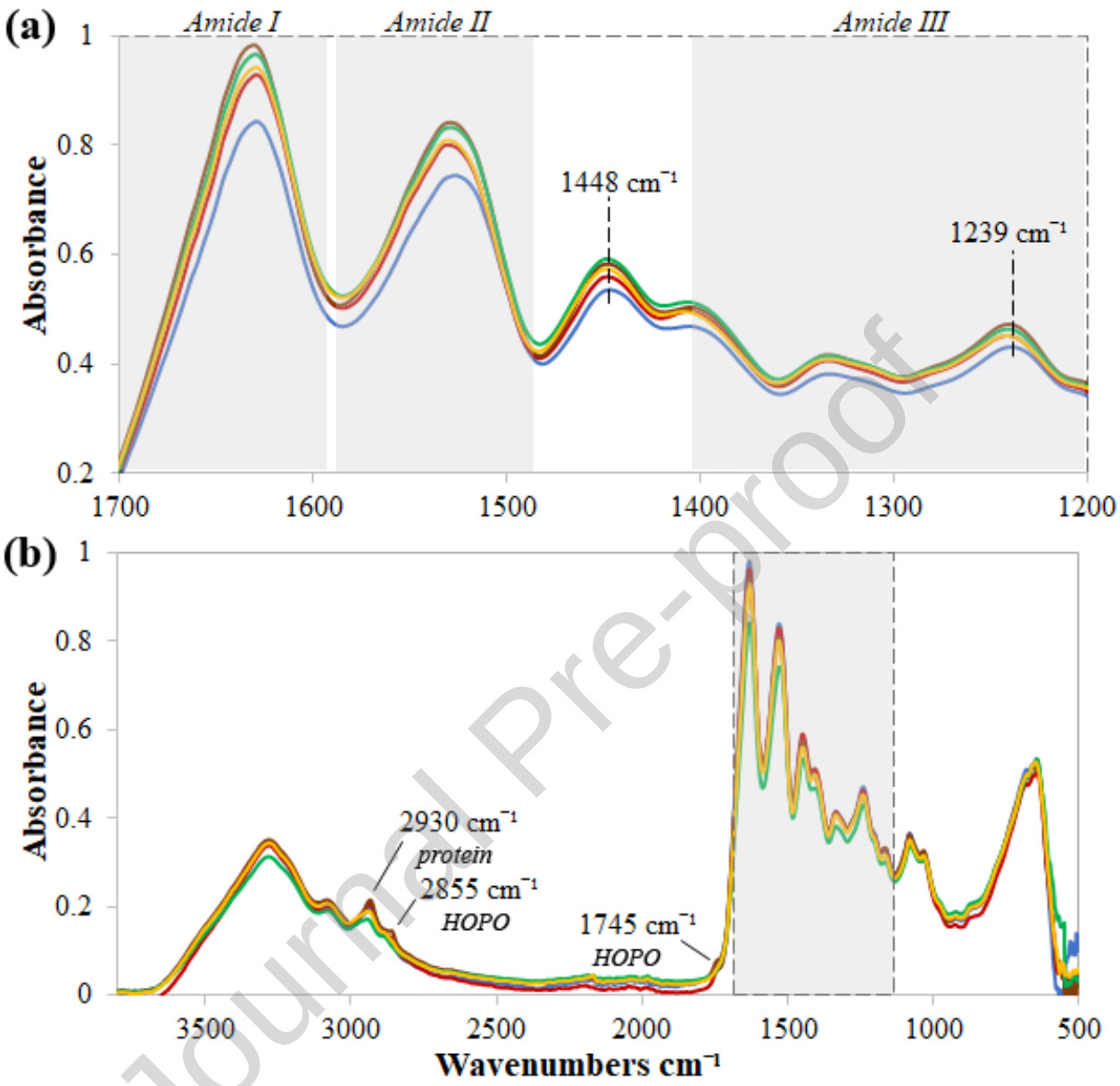

Figure 1S. ATR-FTIR spectra showing **(a)** zoom of amide I, II and III regions and **(b)** characteristic bands from oil of NFs loaded with NE: (—) NF-NE0, (—) NF-NE5, (—) NF-NE10, (—) NF-NE15, and (—) NF-NE20.

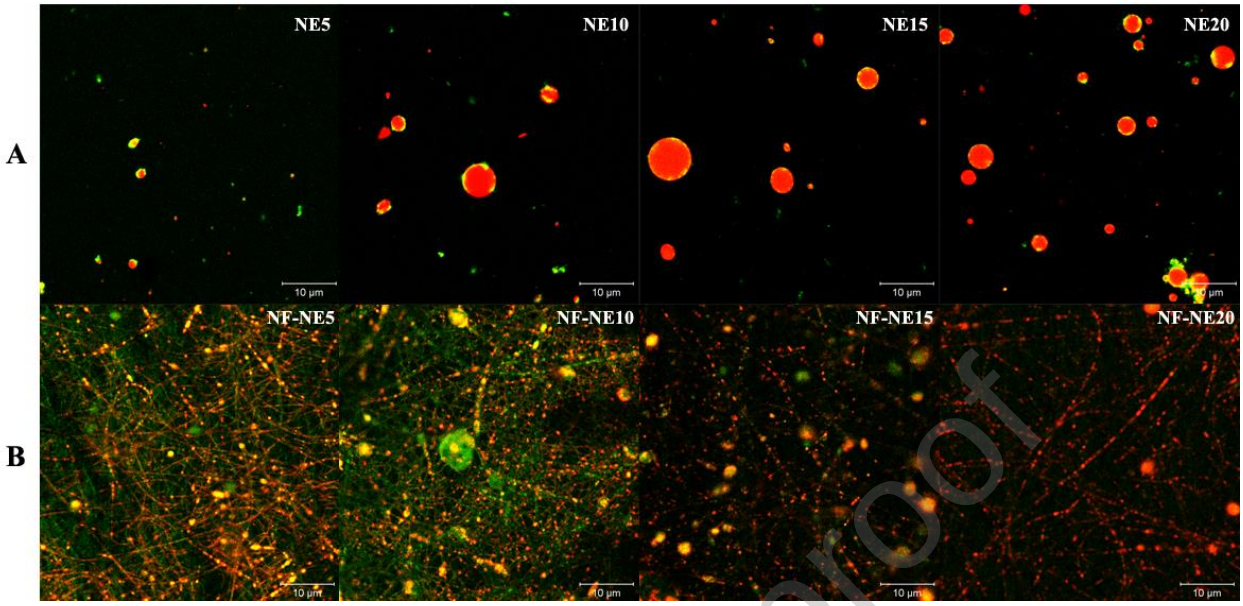

Figure 2S. CLSM micrographs showing colocalization of gelatin protein (green) and HOPO (red) for **(a)** electrospun solutions and, **(b)** NFs loaded with different HOPO concentrations in NEs.

Table 1S. Ranges and average diameters of NFs loaded with different HOPO concentrations in NEs

Sample	HOPO (% w/w)	Range of D_f (nm)		D_f[1] (nm)
		Minimum	Maximum	
NF-NE0	0	49	112	77± 16[a]
NF-NE5	5	57	112	85± 13[b]
NF-NE10	10	65	128	90± 19[bc]
NF-NE15	15	60	115	85± 16[b]
NF-NE20	20	57	130	94± 20[c]

[1]D_f: Fiber diameter

Different letters mean statistical differences ($p < 0.05$) of HOPO concentration in NEs loaded in NF: a, b and c were used

Table 2S. Absorption ratios regarding helical structure of gelatin-based NFs loaded with different HOPO concentrations in NEs

Sample	Absorbance		1235 cm^{-1}:1450 cm^{-1} ratio
	~1235 cm^{-1}	~1450 cm^{-1}	
NF-NE0	0.32± 0.05	0.39± 6E-2	0.81[a]
NF-NE5	0.26± 0.01	0.320± 1E-3	0.80[a]
NF-NE10	0.46± 0.01	0.569± 3E-3	0.80[a]
NF-NE15	0.46± 0.02	0.571± 4E-3	0.80[a]
NF-NE20	0.45± 0.01	0.558± 3E-3	0.81[a]

Same letter means no statistical differences ($p > 0.05$) of HOPO concentration in NEs loaded in NF for each band and ratio analyzed: a, b and c were used